

Energy and Landing Accuracy Considerations for Urban Air Mobility Vertiport Approach Surfaces

Emre Yilmaz*, Matthew M. Warren†, and Brian J. German‡

Georgia Institute of Technology, Atlanta, GA, 30332, U.S.A.

Proposed electric Vertical Takeoff and Landing (eVTOL) aircraft concepts for Urban Air Mobility (UAM) are substantially different than other VTOL aircraft operating today. These design differences imply the need to consider whether changes in aircraft approach and departure procedures and requirements are needed at new eVTOL vertiports compared to existing helicopter operations at current heliports. In this paper, we explore vertiport approach operations for notional eVTOL aircraft in terms of energy consumption and landing accuracy in the presence of atmospheric turbulence.

NOMENCLATURE

$\bar{\mu}$	Normalized Forward Velocity	N_b	Number of Blades
δ	Actuator/Engine Input	p	Roll-Rate
η	Normalized FF contribution to Inflow	Q	Dynamic Pressure
γ	Approach/Climb angle	q	Pitch Rate
λ	Inflow Ratio in Forward Flight	R	Blade Radius
μ	Tip Speed Ratio	r	Yaw Rate
ν	Normalized Induced Velocity	S_b	Rotor Blade Area
Ω	Angular Velocity	S_r	Rotor Disk Area
ϕ	Roll Angle	T	Thrust
ρ	Air Density	u	x_B -axes Velocity
σ	Solidity	V	Total Speed
θ	Pitch Angle	v	y_B -axes Velocity
θ_{TPP}	Rotor Tip Path Plane Angle	v_H	Induced Velocity in Hover
A_π	Equivalent Flat Plate Parasite Drag Area	v_i	Induced Velocity
B	Tip Loss Factor	V_T	Rotor Tip Speed
C_T	Thrust Coefficient	W	Gross Weight
c_{d_0}	Rotor Blade Section Profile Drag Coefficient	w	z_B -axes Velocity
K_{nu}	Correction for nonuniform flow	w_{DL}	Disk Loading

I INTRODUCTION

An emerging vision for Urban Air Mobility (UAM) is based on 4-6 passenger vertical takeoff and landing (VTOL) aircraft with either electric or hybrid propulsion and high degrees of automation that operate in a point-to-point network of “vertiports,” within metropolitan areas. Based on recent and projected advancements in battery specific energy and autonomy capabilities, these VTOL aircraft are anticipated to become feasible in the near term for short

*Graduate Research Assistant, School of Aerospace Engineering, 270 Ferst Drive, and AIAA Student Member.

†Graduate Research Assistant, School of Aerospace Engineering, 270 Ferst Drive, and AIAA Student Member.

‡Langley Associate Professor, School of Aerospace Engineering, 270 Ferst Drive, and AIAA Associate Fellow.

flights of 20-50 miles. Uber has committed to developing an eVTOL UAM network in the Dallas/Fort Worth area and other cities in the near future [1]. Establishing a network of vertiports for UAM operations in urban areas will necessitate aircraft flying and landing near tall buildings and other obstacles within cities.

A practical implementation of UAM operations will require a robust understanding of VTOL approach surfaces and procedures, analogous to the helicopter approach surface example shown in Figure 1 and the approach procedure for off-shore oil rigs explained in Figure 2 to understand their impact on vertiport sizing, safety, and network operations. For UAM, approach surface requirements and associated procedures are anticipated to impact network operational performance in terms of energy expenditure, approach/departure time, and safety.

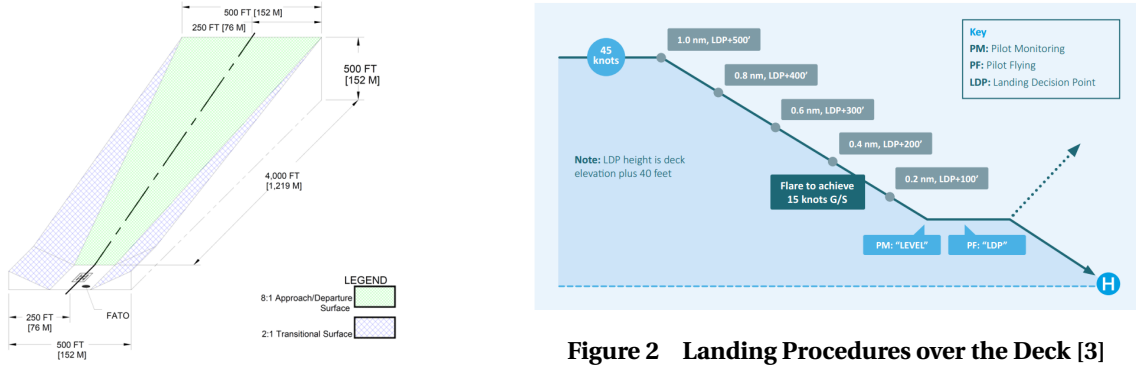


Figure 1 Current Heliport VFR Approach Surface [2]

Figure 2 Landing Procedures over the Deck [3]

Current heliport design standards provide the baseline and starting point for vertiport design and approach and departure surfaces. In *FAA Advisory Circular AC 150/5390-2C Heliport Design* [2], four surfaces are defined for the sizing requirements for heliports and for approach and take-off operations. These surfaces are the takeoff and landing area (TLOF), the final approach and touchdown area (FATO), the approach surface, and the transition surface, as shown in Figure 1. In this document, a distinction is made between different types of heliports, namely, general aviation, hospital, and transport. For general aviation heliports, the minimum width and length of the designated rectangular TLOF and FATO areas are specified as 1 and 1.5 rotor diameter, respectively. Furthermore, the minimum distance from the edge of the VRS safety area to the FATO is designated as one third of the rotor diameter if the TLOF perimeter is marked and half of the overall length of the helicopter if it is not. The document also provides a margin for extra length that should be added to the FATO dimensions when the heliport is situated at altitudes above 1000 ft. Figure 1 shows an approach/departure surface with a glide ratio of 8:1 and a lateral translational surfaces with a glide ratio of 2:1 for general aviation VFR heliports. The surfaces initiate from an elevation of 500 ft and end on the helipad. In *FAA AC 150/5390-2C* [2], the object identification surface has the same glide ratio as the approach/departure surface but with a horizontal distance of 800 ft from the upper edge of the FATO.

In addition to the requirements for these surfaces, procedural guidelines play a crucial role in the determination of approach surfaces and decision points such as in the case for the step down fixes discussed in *the United States Standard for Terminal Instrument Procedures (TERPS)* [4] for IFR flight. Similarly, in [3], landing procedures are provided for off-shore helicopter approach and landings. As shown in Figure 2, these procedures include spatial coordinate checks, the use of a landing decision point, and flare warnings.

In this paper, we present an analysis of landing operations and explore approach surfaces and FATO areas for representative eVTOL UAM aircraft. We model approach in a simple way as flight at constant speed at a constant approach path angle. The approach angles and the corresponding flight speeds are varied to observe the influence on energy expenditure, approach time, and power requirements. Several constraints related to aircraft performance, safety, and operational limits are also posed. These constraints include avoidance of vortex ring state (VRS), approach time limitations, maximum and minimum approach angles, and available power limitations. The influence of high-level eVTOL design parameters such as disk loading on approach performance is also investigated.

For the remainder of the paper, we present results corresponding to a scaled version of the XC-142A, an experimental tilt-wing aircraft tested in the 1960 and 1970s [5] for which a large amount of data is available from NASA reports. The vehicle is scaled to be representative of a 4-6 passenger eVTOL for UAM operations. Scaling is

applied to the stability and control derivatives, dimensions, weight, and propulsion sizing.

A simulation environment was created to model the controlled flight dynamics of the scaled XC-142A. The simulation included a model of atmospheric turbulence based on the Dryden turbulence model. Landing simulations for the selected approach surfaces were run in a Monte Carlo simulation to determine a range of possible landing points. In each individual simulation, the trajectory simulation begins after cruise and transition with the vehicle in hover configuration. The simulation flight path consists of approach at a constant approach angle, a flare, and touch-down. The inner and outer loop structure of the flight control system is designed to control both the approach angle and the speed to desired constant values. The statistical results from the broader Monte Carlo simulation can be used to determine the properties of approach profiles and their applicability to UAM operations based on elliptical error probables (EEPs) for various atmospheric turbulence levels corresponding to different weather conditions.

In the following sections, the overall methodology is provided, and our proposed approach to analyzing the vertiport approach surfaces and FATO dimensions is explained. Next, theoretical background describing the vehicle performance modeling is presented, and constraints on flight performance are introduced. Details about control logic, flight dynamic modeling, and landing simulations are then provided. Finally, results for energy, power, and time subject to various flight dynamics constraints are presented, and elliptical error probables are provided for landing accuracy on the helipad.

II OVERALL METHODOLOGY

Although eVTOL aircraft designed for UAM will likely be far different from existing helicopters, helicopters represent the state of the art in VTOL operations and are the only in-service VTOL aircraft for commercial operations. Therefore, most of the methods employed in this paper stem from the theory of helicopter flight performance. As stated in the introduction, the goal is to explore if and how vertiport sizing should differ from that of existing heliports based on considerations of approach performance and landing accuracy. First, we focus on the analysis of the approach based on vehicle performance and operational constraints. Then, we evaluate the selected approach configurations in terms of landing accuracy with flight dynamics modeling and simulation.

II.A APPROACH SURFACE ANALYSIS BASED ON VEHICLE PERFORMANCE MODELS AND OPERATIONAL CONSTRAINTS

In order to determine feasible landing trajectories that minimize performance indices such as time to land and energy consumption within operational constraints, an approach surface analysis is performed. A landing approach with constant glide slope and constant velocity is assumed to be initiated at 500 ft and to terminate at 50 ft, which is presumed as the altitude at which landing flare is initiated. Glide slope angles in this context represent the approach surfaces on which the vehicle can operate. A grid of angle-speed pairs is defined for the analysis of the landing approach between these two altitudes. The performance metrics that are investigated via this grid of angle-speed pairs are power requirements, energy consumption, and time required along the approach surface.

Several constraints are also considered, including vortex ring state (VRS) boundaries, power available limits, and acceleration limits. The Height-Speed (H/V) diagram is also discussed although it is not anticipated by [6] that H/V considerations will be as relevant as for helicopters because of the low rotor inertia and redundancy of VTOL aircraft with distributed electric propulsion. Additional constraints include obstacle clearance-related considerations.

After deriving energy expenditure and time to reach the flare stage for the grid of angle-speed pairs, subject to constraints, for each descent angle, a speed value that results in minimum energy expenditure is identified from within the feasible regions of the corresponding contours. The feasible trajectories that are represented by these selected pairs of “optimal” speeds and the corresponding angles are then used as reference trajectories for subsequent Monte Carlo simulations of landing accuracy.

II.B DETERMINING LANDING ACCURACY VIA ERROR ELLIPTICAL PROBABLES OF MC SIMULATIONS

In the second analysis presented in the paper, a dynamics simulation environment is created to implement automatic flight control models of the eVTOL aircraft to estimate landing accuracy. The simulations are intended to

support the decision making process for vertiport sizing by providing information about how changing approach angles and speeds influence the landing location on the vertiport surface, presuming that no additional time/energy is spent in terminal-area hover after the approach. Monte Carlo simulations are performed with a linear flight dynamics model for a scaled version of the XC-142A provided by McRuer[5]. Linear models of VTOL A/C for hover, transition, and forward-flight stages are available in [7]. A primary factor that influences the outcome of this landing simulation is the choice of the structure for the inner and outer loops of the controller. For each simulation, the structure is kept the same with the same controller gains so that the selection of each pair is independent of the gains themselves to the greatest extent possible.

III VEHICLE PERFORMANCE

A primary hypothesis of this paper is that high-level vehicle design parameters have a significant effect on energy usage, time, and landing accuracy during approach. In particular, disk loading ($w_{DL} = W/S_r$), solidity ($\sigma = S_b/S_r$), and tip speed ratio ($\mu = V/V_T$) have influence on power requirements and should therefore be taken into consideration. In this section, general assumed ranges for these parameters for eVTOL UAM vehicles are described. Additionally, the rotor geometry for inclined landing, relevant inflow models, and power and energy equations are provided.

III.A RELEVANT DESIGN CHARACTERISTICS OF VTOL UAM VEHICLES

Newly proposed UAM vehicles include many different configurations such as multi-rotors, tilt-wings, tilt-rotors, and lift+cruise vehicles. In our modeling of approach surface effects on flight energy and time, the specific characteristics of the vehicle are not as important as high-level aggregate vehicle parameters such as disk loading. To establish representative values, UAM vehicle data from several sources are collected and then analyzed by fitting curves based on gross weight. These sources include NASA publications[8–10] and technical specifications provided by several companies about their UAM concepts[11–14]. The configurations in NASA publications include not only electric propulsion but also internal combustion engines and hybrid configurations. Figures 3 show the values of empty weight, disk loading, power available, reference drag area, and payload weight plotted against the gross weight. The colors of dots in the figures correspond to the data for NASA concepts and UAM concepts from industrial sources as shown in the legends. Regarding the information obtained from NASA documents, all the platforms with the same configuration but different propulsion units are shown using the same color. The fits to the data are shown as dashed red lines. Based on this data analysis, the specifications shown in Table 1 for three notional but representative UAM platforms were chosen for the subsequent approach performance analysis. These representative platforms are chosen to generally follow the linear trends and/or to be reasonably situated in the scatter of the overall data. These platforms are shown as stars on each figure.

Table 1 Characteristics of Notional UAM Vehicles for Approach Performance Analysis

	GW	W_e	P_A	DL (w_{DL})	$V_{tip,H}$	σ	D/Q
Unit	[lb]	[lb]	[hp]	[lb/ft ²]	[ft/s]	-	[ft ²]
Platform-1	4000	2600	600	6	550	0.1	8
Platform-2	5000	3300	850	8	550	0.1	9.5
Platform-3	6000	3900	1300	10	550	0.1	11.5

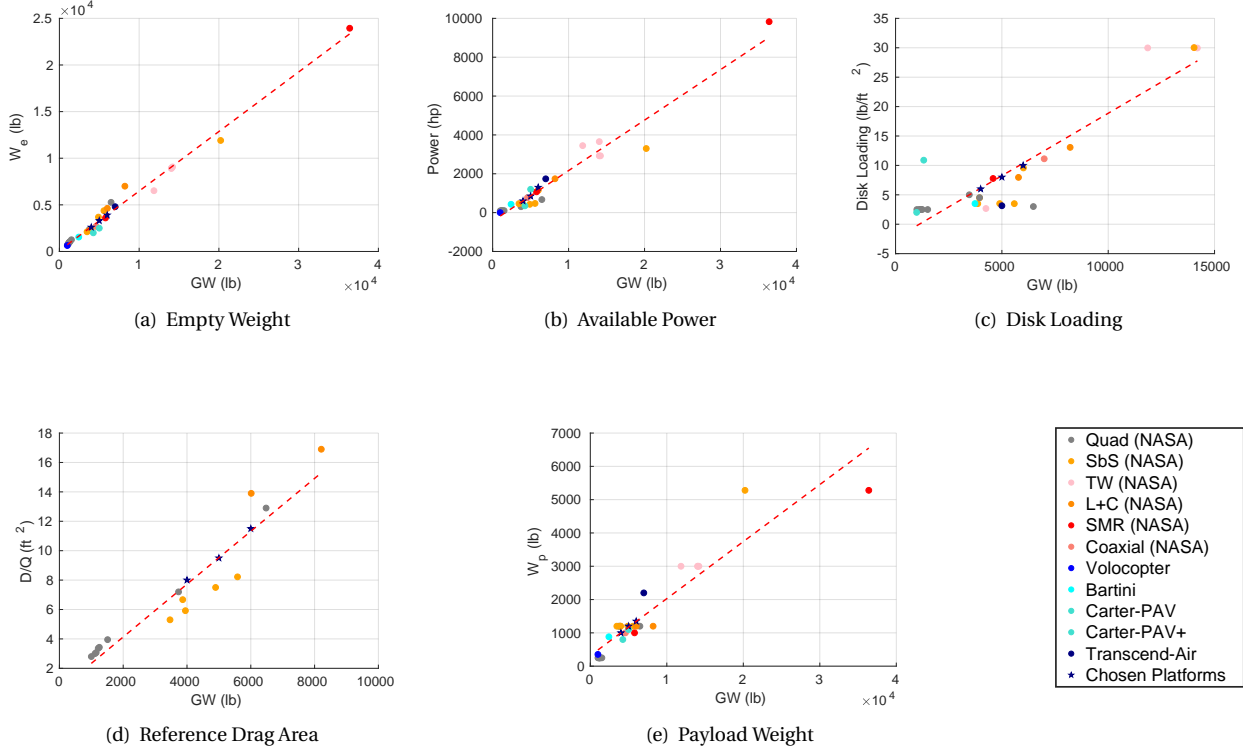


Figure 3 Design Characteristics of Representative UAM Vehicles

III.B GEOMETRY OF INCLINED DESCENT

The geometry of inclined descent during approach involves the rotor tip path plane (TPP) angle (θ_{TPP}), the approach/descent angle (γ), and the angle of attack (α) along with the corresponding equilibria of forces and moments for steady flight. The definitions of these angles and the orientation and the equilibrium of forces are shown in Figure 4, adapted from [15]. The sign convention of tip path plane angle is illustrated in Figure 5. When inspecting photographs and videos of the approach flight path of the V-22, an important aspect that can be noticed is that, in both forward flight descent and vertical descent, these VTOL aircraft maintain very small and slightly positive tip path plane inclinations. Films of flight tests of XC-142A show that this aircraft performs inclined approaches with the wings tilted less than 90 degrees, corresponding to an intermediate between fully rotor-borne and fixed-wing configurations. The main reason for this forward tilt during the inclined descent is to create forward thrust to balance the aerodynamic drag that acts on the platform and to maintain a steady approach with constant forward speed. We assume that the VTOL aircraft considered in this study can perform inclined descent in a rotor-borne state with all the wings or rotors tilted 90 degrees upwards. Flight in this configuration presumes that transition/conversion from fixed wing mode to rotor-borne mode occurs prior to the initiation the constant speed, constant angle descent flight path at 500 ft altitude. We also assume that the tip path plane is tilted slightly forward in order to account for the equilibrium of forces for steady motion in the horizontal direction. With these assumptions, and expressing the angles in terms of their magnitudes in the following formulas, the horizontal and vertical force equilibrium can be written as:

$$\begin{aligned} -W + T \cos(\theta) + D \sin(\gamma) + H \sin(\theta) &= 0 \\ T \sin(\theta) - D \cos(\gamma) - H \cos(\theta) &= 0 \end{aligned} \quad (1)$$

Noting that $\theta = \gamma - \alpha$, an expression for α can be derived as:

$$\tan(\alpha) = \frac{\frac{D}{W \cos(\gamma)} + \frac{H}{T} - \tan(\gamma)}{\frac{D}{W} \frac{H}{T} \frac{1}{\cos(\gamma)} - \frac{H}{T} \tan(\gamma) - 1} \quad (2)$$

Since α is defined as the magnitude of angle of attack, the feasible values that are obtained from this expression should be positive.

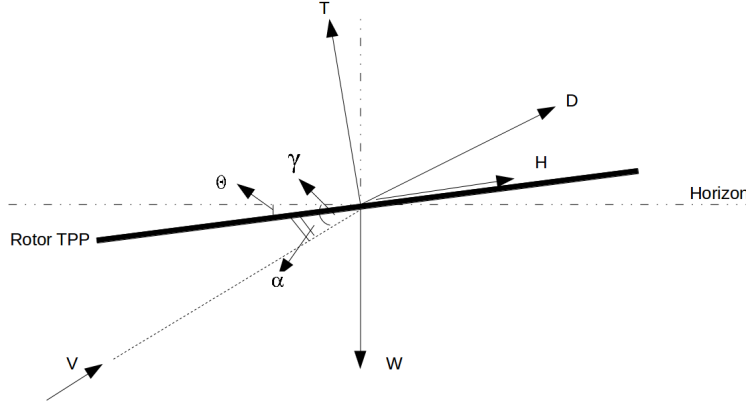


Figure 4 Angles and Forces on a Rotor for the Assumed Orientation in Inclined Descent

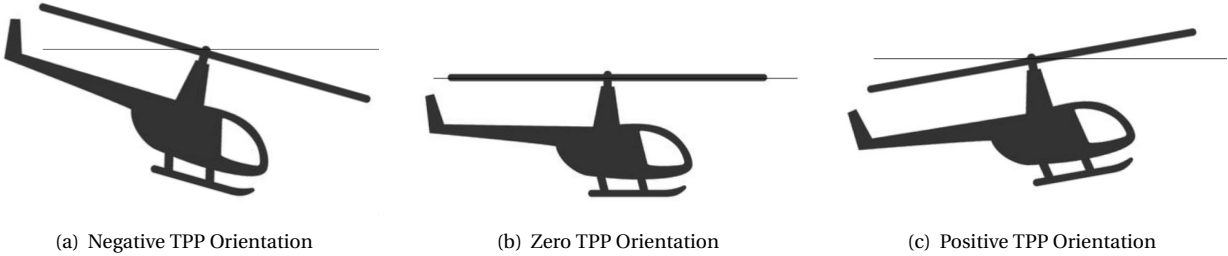


Figure 5 Tip Path Plane Orientation for a Generic Helicopter (silhouette adapted from shutterstock.com)

III.C INFLOW MODEL

An inflow model is necessary for rotorcraft performance analysis and to examine vortex ring state considerations. From simple momentum theory, the hover induced velocity can be defined as:

$$v_H = \sqrt{\frac{T/S_r}{2\rho}} = \sqrt{\frac{w_{DL}}{2\rho}} = \Omega R \sqrt{C_T/2} \quad (3)$$

With the addition of a tip loss factor, the hover induced velocity can be expressed as:

$$v_H = \sqrt{\frac{w_{DL}}{2\rho B^2}} \quad (4)$$

Several definitions for normalized velocities can be specified at this point based on v_H . The normalized induced velocity, the normalized forward velocity, and the normalized form of the contribution of forward flight to the inflow are given in Equations 5 [16]:

$$\begin{aligned} v &= \frac{v_i}{\Omega R \sqrt{C_T/2}} = \frac{v_i}{v_H} \\ \bar{\mu} &= \frac{V \cos(\alpha)}{\Omega R \sqrt{C_T/2}} = \frac{V \cos(\alpha)}{v_H} = \frac{\mu}{\sqrt{C_T/2}} \\ \eta &= \frac{V \sin(\alpha)}{\Omega R \sqrt{C_T/2}} = \frac{V \sin(\alpha)}{v_H} \end{aligned} \quad (5)$$

These normalized terms require tip path plane angles to be zero or negligible as a precondition. In this way, angle of attack and approach angle can be used interchangeably. Otherwise, the influence of the tip path should be included as explained in [15] with the assumption that the rotor wake does not change its orientation from the reference frame perpendicular to the rotor plane. Finally, the inflow ratio in forward flight is $\lambda = \eta + v$. The focus of this paper is an inclined descent rather than the hover case; therefore, simple momentum theory in forward flight is expressed next.

$$T = 2\rho S_r v V_T \quad \text{where} \quad T = 2\rho S_r v_H^2$$

$$v_i = \frac{T/(2\rho S_r)}{\sqrt{(V\cos(\gamma))^2 + (V\sin(\gamma) + v_i)^2}} \quad (6)$$

From momentum theory, the following quartic equation for the solution of induced velocity is obtained [15] :

$$v_i = \frac{v_H^2}{\sqrt{(V\cos(\gamma))^2 + (V\sin(\gamma) + v_i)^2}}$$

$$1 = \frac{v_i}{v_H} \sqrt{\left(\frac{V\cos(\gamma)}{v_H}\right)^2 + \left(\frac{V\sin(\gamma)}{v_H} + \frac{v_i}{v_H}\right)^2}$$

$$1 = v \sqrt{\bar{\mu}^2 + (\eta + v)^2}$$

$$0 = v^4 + 2\eta v^3 + (\eta^2 + \bar{\mu}^2)v - 1 \quad (7)$$

There also exist other modified forms of this quartic equation. Momentum analysis of inclined descent [17] results in a version for inclined descent as follows:

$$v^4 + 2(\eta + \bar{\mu}\tan\gamma)v^3 + (\eta^2 + \bar{\mu}^2)v - 1 = 0 \quad (8)$$

In this paper, a modified form described by Chen[16] that includes the steady state transition from the helicopter branch to the windmill brake branch that appears in the solution of simple momentum theory is used for subsequent analysis:

$$v^4 + 2\eta v^3 + \left(\eta^2 + \bar{\mu}^2 + \frac{\eta^2}{(2.72(1 + \bar{\mu}^2))^2}\right)v - 1 = 0 \quad (9)$$

III.D POWER AND ENERGY CALCULATIONS

Two methods for exploring the performance of rotocraft in descent are the energy and force balance approaches[15]. For power calculations, we use the energy balance method with several assumptions that are discussed in the following sections. The following power model described in [18] for rotocraft is assumed to be appropriate for this analysis. This approach does not include effects associated with the interference of rotor wake with wings, which are likely important for tilt-wing vehicles such as our scaled XC-142A reference model. For further modeling of such considerations at a conceptual design level, software such as NDARC [19] could be used. The power breakdown assumed in this analysis can be expressed as follows:

$$hP_{\text{all}} = hP_i + hP_r + hP_p + hP_{c/d} \quad (10)$$

where hP_{all} is total power, hP_i is induced power, hP_r is rotor profile power, hP_p is parasite power, and $hP_{c/d}$ is additional power term due to climb or descent, all expressed in horsepower. Several assumptions can be made at this point about how to expand each of these terms.

First, an inflow model that depends on modified momentum theory is used. Non-uniform flow, reverse flow, tip loss, and radial drag effects are included as correction terms. All descent profiles are assumed to have a constant descent rate, constant velocity, and thus constant straight glide path. Small angles assumptions are made for the tip path plane, and force equilibrium is derived based on these assumptions. Equation 11 defines the induced power term with non-uniform flow and tip loss factor corrections.

$$hP_i = K_{\text{nu}} \frac{T}{550} v_i = K_{\text{nu}} \frac{T}{550} v v_H = K_{\text{nu}} v \frac{T}{550} \sqrt{\frac{w_{DL}}{2\rho B^2}} \quad (11)$$

where non-uniform flow correction can be assumed to be $K_{nu} = 1.13$ for a triangular flow distribution, and the tip loss factor is modeled as $B = 1 - \sqrt{2C_T}/N_b$.

Rotor profile power is given as,

$$\begin{aligned} hP_r &= K_\mu \frac{1}{550} \frac{T}{w_{DL}} \frac{\sigma c_{d0}}{8} \rho V_T^3 \\ &= K_\mu \frac{1}{550} T \left(\delta_0 \frac{\rho V_T^3}{8w_{DL}/\sigma} + 36\delta_2 \frac{w_{DL}/\sigma}{8\rho V_T C_{L_\alpha}^2} \right) \end{aligned} \quad (12)$$

where K_μ accounts for the power rise due to asymmetry in forward flight. There exist different models for this rise as a function of tip speed ratio, μ that are valid for different intervals of μ and that can also include considerations related to reverse flow and retreating blade stall. For example, a simple model with such corrections is given as $K_\mu = 1 + 4.6\tilde{\mu}^2$. The drag polar can be assumed as $c_{d0} = \delta_0 + \delta_2 \alpha_r^2$ where α_r is rotor blade angle, and δ_0 and δ_2 are parameters of the drag polar that can either be assumed constant or that can change based on rotor angles and operating conditions. Finally, the parasite power is given as,

$$hP_p = A_\pi Q \frac{V}{550} = \rho A_\pi \frac{V^3}{1100} \quad (13)$$

where $A_\pi = D_p/Q$ values can be taken from the literature as shown in Table 1 or from a drag build up method for a specified platform. The $V_{cl/d}$ term is either the climb power required to gain altitude and potential energy or the extra power obtained for the potential energy loss in descent. A simple approach is to approximate this term as the product of weight and the climb/descent rate. For a given approach surface with constant angle, γ , and a constant vehicle speed, V , the energy can be calculated as $E_{req} = P_{req}\Delta t$ where the time increment, Δt , is a function of γ and V .

IV CONSTRAINTS ON FLIGHT PERFORMANCE AND OPERATION

Take-off, approach, and landing procedures place constraints on the trajectory tracking logic and precision navigation of VTOL aircraft. These restrictions have their roots in flight physics, vehicle performance, and operation-related limitations. Therefore, it is vital not only to keep track of these constraints in our simulations but also to plan the approach profiles and the landing operation according to these constraints. The vortex ring state region, the regions that should be avoided in the H/V diagram based on considerations of autorotation and pilot reaction time, acceleration limits associated with passenger comfort, and available power limitations are among these flight and vehicle performance related constraints.

IV.A HEIGHT VS. VELOCITY DIAGRAM (DEAD MAN'S CURVE)

For traditional helicopters, height vs. airspeed (H/V) diagrams, also known as Dead Man's Curves, indicate unsafe regions of operation in the flight envelope. A representative diagram is shown in Figure 6 for a helicopter [?]. The unsafe part on the left of the Dead Man's Curve in Figure 6 indicates insufficient energy to convert into autorotation and to arrest the descent rate, whereas the section on the right bottom side is a high speed constraint referring to insufficient time to flare and arrest kinetic energy [6]. With the introduction of distributed electric propulsion concepts in UAM, the autorotation region on the left hand side of H/V diagrams may be presumed to disappear in cases in which there is redundancy in both actuation and energy supply to the propellers/actuators. When one rotor fails, other rotors remain functional and continue the operation in a fault tolerant setting. Furthermore, each rotor may be presumed to be connected to multiple batteries through independent electrical buses for safety. Fredericks argued that UAM vehicle designs may negate the need to consider the Dead Man's curve in the same ways as for traditional helicopters [6]. However, each different configuration requires a different analysis and risk mitigation strategy. For example, some design concepts with low rotor inertia and fixed pitch rotors will not be capable of preserving potential energy and converting it into kinetic energy of the rotor to enable autorotation, whereas other concepts with variable pitch rotors of a larger size might enable autorotation. Assuming a similar H/V diagram is suitable for these latter types of UAM aircraft as for single main rotor helicopters, the regions to be avoided appear as a minimum velocity requirement in the low speed region and a maximum velocity requirement in the high speed region for a given altitude.

IV.B VORTEX RING STATE

Vortex ring state (VRS) is a significant aerodynamic phenomenon that can happen during the descent of a rotorcraft as a rotor flies into its own downwash. This phenomenon leads to large vibrations and uncontrolled descent profiles. From a pilot's perspective, VRS can be described as a sudden feeling of lightness in the control of the vehicle and then uncontrolled fall and push-down to the ground. VRS puts serious constraints on the maximum rate of descent that can be employed in an inclined approach or hover landing of VTOL aircraft. Avoiding VRS may lead to excessively long vertical descent times. As a strategy against entering this region, helicopters typically descend along an approach angle rather than vertically. A design parameter that can significantly affect VRS is disk loading. Vehicles with higher disk loading lose altitude quicker after entering VRS and might lack the time needed to escape the phenomenon via techniques such as the Vuichard recovery [21].

Since many newly-designed UAM vehicles are multi-rotors, a valid question is the applicability of VRS to multi-rotors. VRS is indeed applicable to multi-rotors, and it is common for multi-rotors to become unstable as different rotors enter vortex ring and then shed the vortex [22]. Similarly, tilt-rotors such as the V-22 exhibit “roll-off” behavior [23]. Some questions remain about effects of vortex ring on vehicles with substantial interference effects such as the Volocopter [24].

VRS boundaries indicate a region of danger and should therefore be integrated as constraints into our approach performance analysis. The pilot's manual ([20]) for the Robinson R22, which has a disk loading of $2.6 \text{ lb}/\text{ft}^2$, suggests a vertical descent rate of no more than $300 \text{ ft}/\text{min}$.

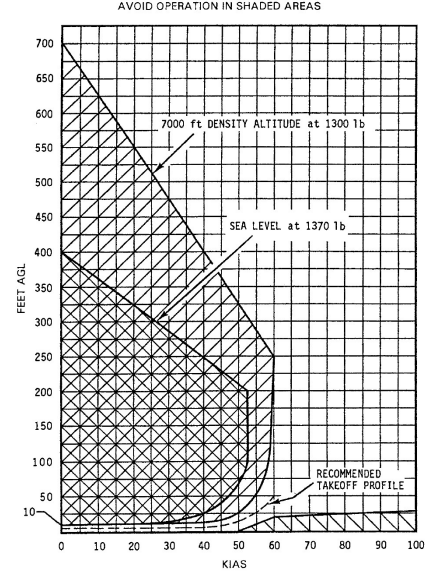
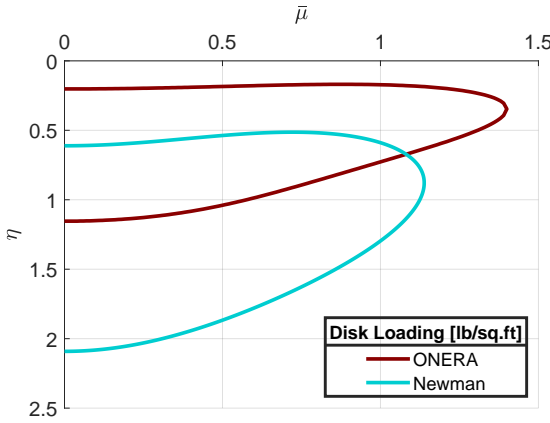
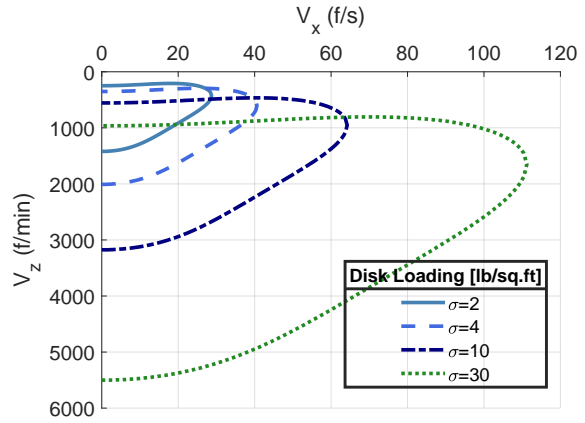


Figure 6 Height vs. Airspeed (H/V) Diagram for a Helicopter [20]

Vertical airspeed (V_z) vs. horizontal airspeed (V_x) for various disk loadings (σ). The plot shows V_z (f/min) on the y-axis (0 to 6000) and V_x (f/s) on the x-axis (0 to 120). Four curves are shown for different disk loadings:



(a) The Comparison of Different Boundaries



(b) The Change of ONERA's Boundary[25] with Disk Loading

Figure 7 VRS Boundaries for Various Disk Loadings

Several references on helicopter theory [15, 16, 25, 26] provide guidelines and heuristics for the boundaries of the vortex ring state in vertical descent. For example, Newman's wake transport criterion for VRS assessment[26] provides a boundary for the onset of flow breakdown in the wake stream tube represented by $\bar{\mu}_{\text{crit}}$. The boundaries can be expressed as $\eta = \pm \sqrt{\bar{\mu}_{\text{crit}} - k^2 \bar{\mu}_x^2} - \bar{\mu}_{WT}^{-1}$ where the true wake transport velocity is $\bar{\mu}_{WT} = \sqrt{\bar{\mu}_{\text{crit}} - (1 - k^2) \bar{\mu}_x^2}$. In his work, Newman assumed that $k = 0.65$ and $\bar{\mu}_{\text{crit}} = 0.74$. ONERA [25] developed a semi-empirical formula for the estimation of the proximity of a vehicle in a flight condition to VRS. This closeness metric designated by ϵ is given as $\sqrt{\frac{\bar{\mu}^2}{16} + (\eta + 0.5v)^2}$. A value below $\epsilon = 0.25$ points out the existence of fully developed vortex rings and VRS

[27]. Therefore, the region where $\epsilon \leq 0.35$ is assumed to be a conservative zone that includes the VRS zone that needs to be avoided. These two boundaries are shown in Figure 7(a) in terms of normalized velocities. Figure 7(b) includes the change of ONERA boundaries for various disk loading values.

IV.C ACCELERATION, AVAILABLE POWER, AND OBSTACLE CLEARANCE LIMITATIONS

Early studies of human response to motion and turbulence in vehicles were carried out in the marine [28] and aerospace fields [29–31]. The studies about marine vehicle ride quality are based on surveys about the vulnerability of humans to motion sickness. In aerospace studies, the primary concerns have been noise, vibration, and vertical accelerations. All these studies have aimed to predict crew or passenger comfort boundaries. In this paper, we include boundaries corresponding to maximum negative acceleration limits applied to the passengers during the flare stage in order for the vehicle to slow down and then come to a stop on the landing pad. For the results section, the magnitude of the deceleration limit during flare stage is chosen as 0.1 g's based on the guidelines in [32].

Available power also acts as a constraint and indicates a region where the propulsion unit cannot meet the operational power requirements.

The required obstacle clearance (ROC) above the obstacle clearance surface (OCS) discussed in TERPS serves as limit to the minimum approach and departure angles. Required obstacle clearance surfaces for a vertiport can be determined from several factors such as buildings along the flight landing/departure paths. In case there exist more than one approach surface to a vertiport, each surface will have its own minimum required obstacle clearance value.

V FLIGHT DYNAMICS MODELING AND SIMULATION

In order to develop an understanding of landing accuracy and the dimensions on the vertiport FATO area, flight dynamics modeling is conducted and a simulation environment is created. This simulation environment for VTOL aircraft includes flight dynamics modeling of the aircraft, automatic flight control system (AFCS) design, landing and flare procedures, assumptions about sensor feedback, and an atmospheric turbulence model to simulate the effects of weather. The simulations are based on the aforementioned scaled XC-142 model. The stability and control derivatives of the XC-142A presented in McRuer[5] are scaled for modeling the flight dynamics. Franklin [7] provides linearized dynamics models around trim conditions for hover, transition, and forward flight.



(a) Tilt-Wing Concept: XC-142A [33]

Figure 8 Experimental VTOL aircraft from 1960/70s used as baseline for scaling to UAM concepts

V.A MODEL SCALING

The flight dynamic models obtained from the data in McRuer[5] and the descriptions in Franklin[7] are scaled and modified to match the currently-envisioned eVTOL aircraft concepts for UAM. The stability and control

derivatives are assumed to be linear combinations of force and moment coefficients, say \tilde{C} [34]. The rate of proportionality of these combinations to flight derivatives is a function of dimensions(d), areas(S), volumes(Λ), weights(W), inertia(I), flight conditions(V), and dynamic pressure(Q) as shown in the following representative equation for the stability derivative X_u :

$$X_u^{\text{original}} = \kappa(d, S, \Lambda, W, I, V, Q) \tilde{C} \quad (14)$$

In order to scale the XC-142A to a size appropriate for UAM, we define scaling ratios for dimensions and weight.

$$X_u^{\text{scaled}} = \frac{\kappa(d^{\text{scaled}}, S^{\text{scaled}}, \Lambda^{\text{scaled}}, W^{\text{scaled}}, I^{\text{scaled}}, V, Q)}{\kappa(d, S, \Lambda, W, V, Q)} X_u^{\text{original}} \quad (15)$$

Several strong assumptions are made when scaling the tilt-wing aircraft model. First, the combination of coefficients are assumed to remain the same and thus preserve their characteristics when scaled. As previously mentioned, derivatives can be expressed as linear functions of coefficients and the rate of proportionality is a function of dimensions, areas, volumes, masses, inertia, and operation conditions [34]. Dimensions, areas, and volumes can be scaled based on the respective powers of dimensional scaling ratios. Mass and inertia can be scaled similarly either by assuming an unchanged mean vehicle density when scaled or via an independent mass scaling ratio. The resulting wing loading values obtained from this procedure should be checked to verify that they are plausible for UAM vehicles. The resulting scaling of control derivatives related to the rotors should also be checked post facto. The vehicle platforms specified in the previous section are used as baselines for scaling to generate the results in this paper.

V.B LINEARIZED DYNAMIC FLIGHT MODELS FOR SIMULATIONS

For the equations of motion, 6-DOF decoupled linearized rigid body dynamic models are used based on the hover, transition, and forward flight models for VTOL A/C described in Franklin [7]. Longitudinal and lateral state vectors can be defined as $x_{\text{long}} = [u, w, q, \theta]^T$ and $x_{\text{lat}} = [v, p, \phi, r]^T$, respectively. The wind gust vectors that provide the influence of turbulence models on the system are represented by $x_{\text{lon},w}$ and $x_{\text{lat},w}$. The linearized dynamics equations can be expressed as follows:

$$\begin{aligned} \dot{x}_{\text{lon}} &= A_{\text{lon}}(x_{\text{lon}} + x_{w,\text{lon}}) + B_{\text{lon}} u_{\text{lon}} \\ \dot{x}_{\text{lat}} &= A_{\text{lat}}(x_{\text{lat}} + x_{w,\text{lat}}) + B_{\text{lat}} u_{\text{lat}} \end{aligned} \quad (16)$$

where the system and control matrices change according to flight condition. For example, for hover where the wings of the tilt-wing aircraft are tilted 90 degrees and the VTOL aircraft is in a rotor-borne configuration, the corresponding matrices are given in Equations 17:

$$\begin{aligned} A_{\text{lon},H} &= \begin{bmatrix} X_u & 0 & 0 & -g \\ Z_u & Z_w & 0 & 0 \\ M_u & M_w & M_q & 0 \\ 0 & 0 & 1 & 0 \end{bmatrix} & B_{\text{lon},H} &= \begin{bmatrix} X_{\delta s} & X_{\delta T} \\ Z_{\delta s} & Z_{\delta T} \\ M_{\delta s} & M_{\delta T} \\ 0 & 0 \end{bmatrix} \\ A_{\text{lat},H} &= \begin{bmatrix} Y_v & 0 & g & 0 \\ L'_v & L'_p & 0 & L'_r \\ 0 & 1 & 0 & 0 \\ N'_v & N'_p & 0 & N'_r \end{bmatrix} & B_{\text{lat},H} &= \begin{bmatrix} Y_{\delta P} & Y_{\delta A} \\ L'_{\delta P} & L'_{\delta A} \\ 0 & 0 \\ N'_{\delta P} & N'_{\delta A} \end{bmatrix} \end{aligned} \quad (17)$$

Table 2 contains the assumed set of longitudinal and lateral derivatives obtained after scaling in rotor-borne configuration.

Table 2 Stability and Control Derivatives of Scaled Tilt-Wing Aircraft

X_u [s ⁻¹]	-0.4295	Z_u [s ⁻¹]	0	M_u [rad/ft/s]	0.0286
X_w [s ⁻¹]	0	Z_w [s ⁻¹]	-0.1329	M_w [rad/ft/s]	0.0012
X_q [ft/s/rad]	-3.7608	Z_q [ft/s/rad]	0	M_q [s ⁻¹]	-0.1783
$X_{\delta s}$ [ft/s ² /in]	0	$Z_{\delta s}$ [ft/s ² /in]	5.2767	$M_{\delta s}$ [rad/s ² /in]	3.0147
$X_{\delta T}$ [ft/s ² /deg]	0	$Z_{\delta T}$ [ft/s ² /rad]	-24.3383	$M_{\delta T}$ [rad/s ² /rad]	0.1018
Y_v [s ⁻¹]	-0.0307	L'_v [rad/ft/s]	-0.0023	N'_v [rad/ft/s]	-0.0015
$Y_{\delta A}$ [ft/s ² /in]	0	$L'_{\delta A}$ [rad/s ² /in]	-1.1158	$N'_{\delta A}$ [rad ft ⁻¹ s ⁻¹]	-0.0126
$Y_{\delta P}$ [ft/s ² /in]	0	$L'_{\delta P}$ [rad/s ² /in]	0.2764	$N'_{\delta P}$ [s ⁻¹]	-0.8144
$L'_{\delta r}$ [rad/s ² /in]	0.2435	L'_p [s ⁻¹]	-0.4806	N'_p [s ⁻¹]	-0.0126
$M_{\dot{w}}$ [rad/ft]	-0.0027	L'_r [s ⁻¹]	-0.0685	N'_r [s ⁻¹]	-0.4315

V.C DRYDEN WIND TURBULENCE MODEL

Turbulence modeling for simulations of helicopters include frozen field and rotating frame models [35–38]. In this paper, we assume that the Dryden wind turbulence model is valid for the purpose of our simulations since we investigate a case where we have an inclined descent with a forward component of the velocity. The frozen field assumption gives relatively more reliable results as long as the vehicle is not at hover or very low speeds where the basic assumptions break down [35]. The uncertainties related to weather conditions are therefore included in simulations via a Dryden turbulence model which can be interpreted as a way to handle the gusts as stochastic processes based on power spectral densities. Via spectral factorization, the corresponding transfer functions for the influence of continuous gusts on linear and angular velocity components of the vehicle can be obtained and thus the wind turbulence can be simulated via a white noise input to these functions in the frequency domain [39].

V.D FLIGHT CONTROL STRUCTURE

Several levels of automation in an advanced AFCS architecture are created for simulations. The inner-most loop controls the flight dynamics whereas the outer loops give commands to the inner loop based on the guidance logic, sensor data, and deviations from desired trajectories. Full state feedback is assumed for all the simulations. In the inner-most loop of the control architecture, an error feedback control is used to stabilize the unstable modes for both lateral and longitudinal dynamics. The gains of the feedback control are selected via the LQR method. Attitudes and body velocities of the platform are closed in this loop. Commands to change these states are provided by an outer loop where the guidance logic is managed. The constant speed, constant angle approach trajectory is dictated by this loop to the inner loop via the calculation of command speeds and angles. The path following logic for flight control is designed to ensure that the aircraft remains on the approach surface. As a strategy to avoid deviations from the glide slope, a spatial correction term is also included in the commands to the inner loop. The use of glide slope hold by itself might require gain scheduling or an optimization routine for fine tuning and will most likely result in significant deviations from desired approach surface. The corrective module penalizes the distance from the reference trajectory obtained via sensors. The influence of the addition of this deviation rejection module to the glide slope hold is shown in Figure 9.

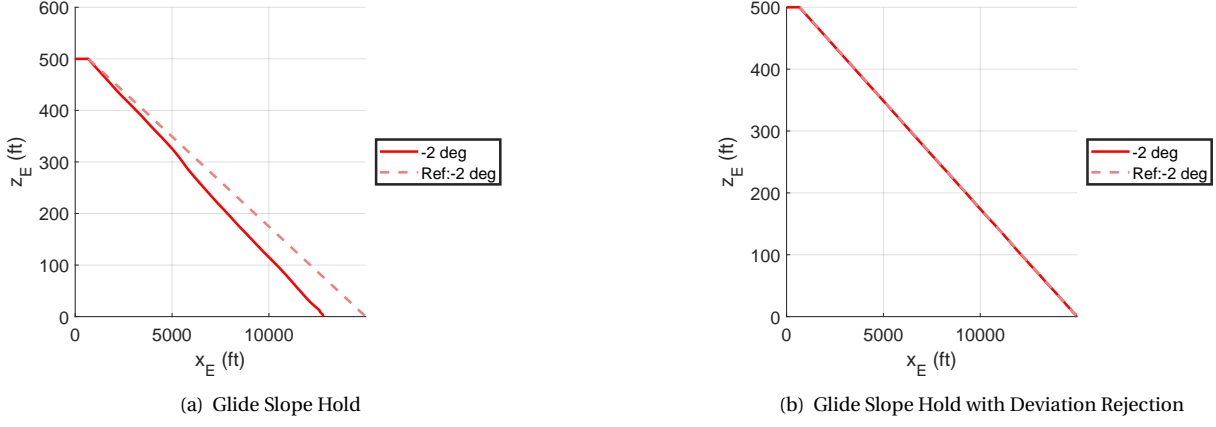


Figure 9 The Influence of Corrective Action

The outer loop has switching modules for flare, approach, and cruise segments. For example, the flare stage is assumed to be initiated when the vehicle reaches 50 ft elevation. In the flare, the vehicle stays on the same glide slope but decreases its velocity step by step based on the the elevation.

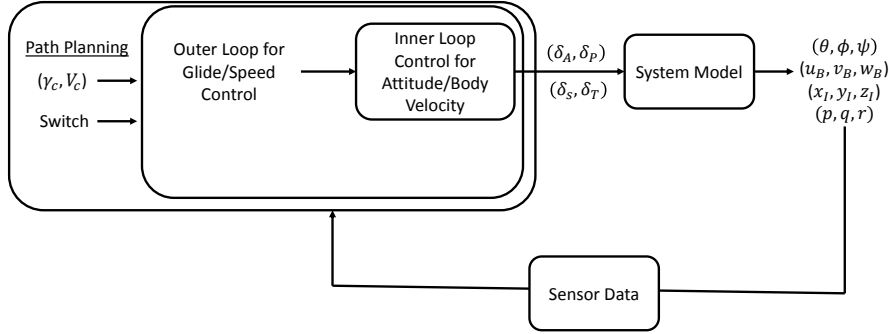


Figure 10 Diagram for Flight Control System and Model

VI RESULTS AND DISCUSSION

The results are discussed in two main parts: performance analysis and landing accuracy simulations.

VI.A PERFORMANCE ANALYSIS RESULTS

We first evaluate VRS, acceleration, procedure, and vehicle performance constraints to develop a set of approach surface and speed pairs that gives favorable outcomes in terms of performance metrics. The resulting pairs are then applied to the full simulation for evaluating landing accuracy. The performance analysis is carried out for the three platforms discussed in Table 1. Figures 11 show the maps for power required terms calculated for Platform 1. Induced power is the most dominant term with a higher distribution of values toward the right middle section of the plot. Profile power is the second most dominant term with increasing behaviour towards lower descent angles and higher velocities. Parasite power calculations are generally lower and might be optimistic as a result of the assumed approach. Interference terms are not included; however, based on the configuration of the UAM vehicle, interference effects may have non-negligible influence over total power required.

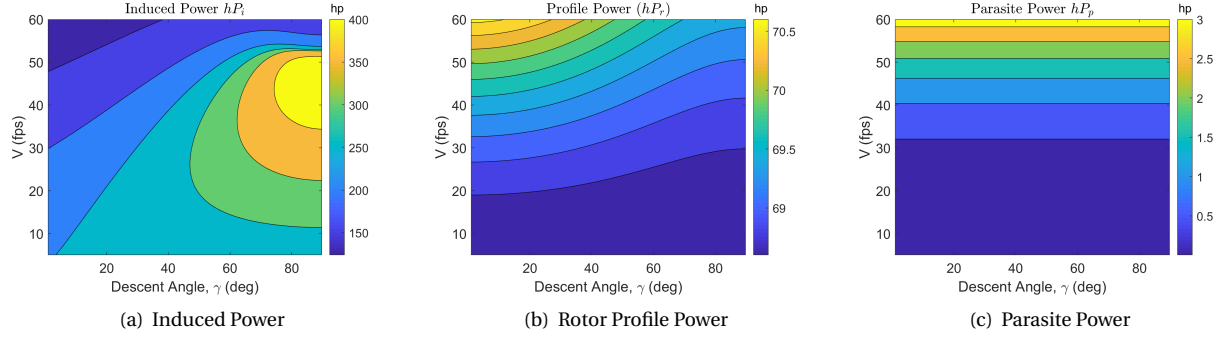


Figure 11 Maps for Required Power Terms for Platform 1

Figures 12 show the power contours for the selected platforms during the landing approach. The first observation can be made for VRS boundaries. As the disk loading increases, the VRS zone becomes larger in size and extends along the acceleration constraint boundaries, covering larger portions of the domain of speeds and descent angles. The zone itself also shifts slightly upwards. For descent angles less than around 5 deg, no constraint is active. Around 5 degrees of γ , 0.1-g acceleration limit initiates as the first dominant constraint which is followed by the dominance of the VRS boundary starting from around 10 degrees of γ . It is worthwhile to note that available power does not appear in these figures because of the relatively lower power requirements. Figure 13 shows contours of energy and time to reach flare from the initiation of the landing approach. The same considerations discussed for power contours are valid for energy contours which are shown in Figures 13(a), 13(c), and 13(e) as well. The energy expenditure is at its highest value around origin and decreases towards the boundaries. Therefore, the minimum energy solution of the map is expected to be at the intersection of the active constraints. For the time contours shown in Figures 13(b), 13(d), and 13(f), two extra conditions for the maximum and minimum allowable time spent on the approach surface are added to the set of constraints. The minimum limit is set to 1.5 minutes and the maximum limit is assumed as 10 minutes based on considerations of reasonable of safety and mission pace. The trends observed in the time required contours are similar to the ones in the energy contours. The feasible region of the time contours in the velocity-descent angle domain covers the area in between the two boundaries for the maximum and minimum time limits. The minimum time and minimum energy solution is expected to be on this min-time boundary which dominates the influence of the VRS and acceleration boundaries.

Figure 14 indicates the values of speed for given descent angles that give the minimum energy requirements along the approach surface and the corresponding energy requirements without violating the constraints. At lower descent angle values, the minimum energy solution is at the highest achievable and safe velocity. As the descent angle increases, the solution moves on the acceleration constraint to finally jump to the VRS boundary at the intersection of both constraints. As the angle is further increased, the solution is obtained on the lower part of VRS region.

All the figures mentioned up to this point do not include considerations for potential energy loss or the extra power required to gain altitude. Next, we compare the total power for Platform 3, also including these terms in a simple manner as $WV_{c/d}$. Positive γ represents climb and results in more power required for the necessary potential energy gain to climb to a higher altitude. The extra positive term, $P_{c/d}$, is this power required to climb. In this case, the power available constraint needs to be considered as well because of the extra power requirements. The infeasible region in terms of power availability appears for higher speed and angle values at the right top corner of the plot. During landing approach, which is the focus of this work, this term results in less power required due to potential energy loss and is negative. Therefore, this term acts to relax the power requirements.

The power contours for these additional terms are shown in Figures 16(a) and 16(b) and the energy contours for the descent case are shown in Figure 16(d). Since the minimal-energy curves do not change for the descent case with the addition of potential energy losses, Figures 14 are still valid with corresponding values as in Figure 15. As explained previously, it might be possible to neglect the constraints in H/V diagrams based on assumptions that assure safety in case of a motor failure in a distributed electric propulsion aircraft. However, if we assume that autorotation capability will still be a key factor for certain aircraft configurations, it is valuable to investigate the influence of adding constraints related to the low and high speed zones in H/V diagrams to our power, energy, and time contours. We assume that the H/V diagrams for these platforms are similar to helicopter diagrams. Under

this assumption, two different types of constraints might occur for a specified height. First, the low-speed region in which operation should be avoided due to the absence of adequate kinetic energy in the case of an autorotation, dictates a minimum speed boundary. Secondly, the high speed region which should be avoided due to the absence of time to respond to in case of an emergency gives a maximum speed boundary, generally quite close to the ground. In addition to appearing by themselves, for some heights, both of these maximum and minimum speed constraints coexist. This leads to an allowable region of operation in between both speeds. Figure 17(a) shows the representative addition of a maximum speed limit of 50 ft/s for a generic altitude. This limit constricts the feasible space from lower descent angles. All descent angles are still achievable. Figure 17(b) represents the limitations from the low speed region and shows the addition of a minimum speed limit of 25 ft/s for another generic altitude. This case appears to be severely restrictive, constraining the feasible space to the upper left portion of the domain. The lower part of VRS boundary is no longer active and the descent angles greater than either the intersection of VRS boundary and minimum speed limit from the H/V diagram or acceleration limit are not achievable. Finally, Figures 18(a) and 18(b) show power and energy expenditure considerations with the addition of a minimum angle speed constraint dictated by required obstacle clearance and obstacle clearance surface.

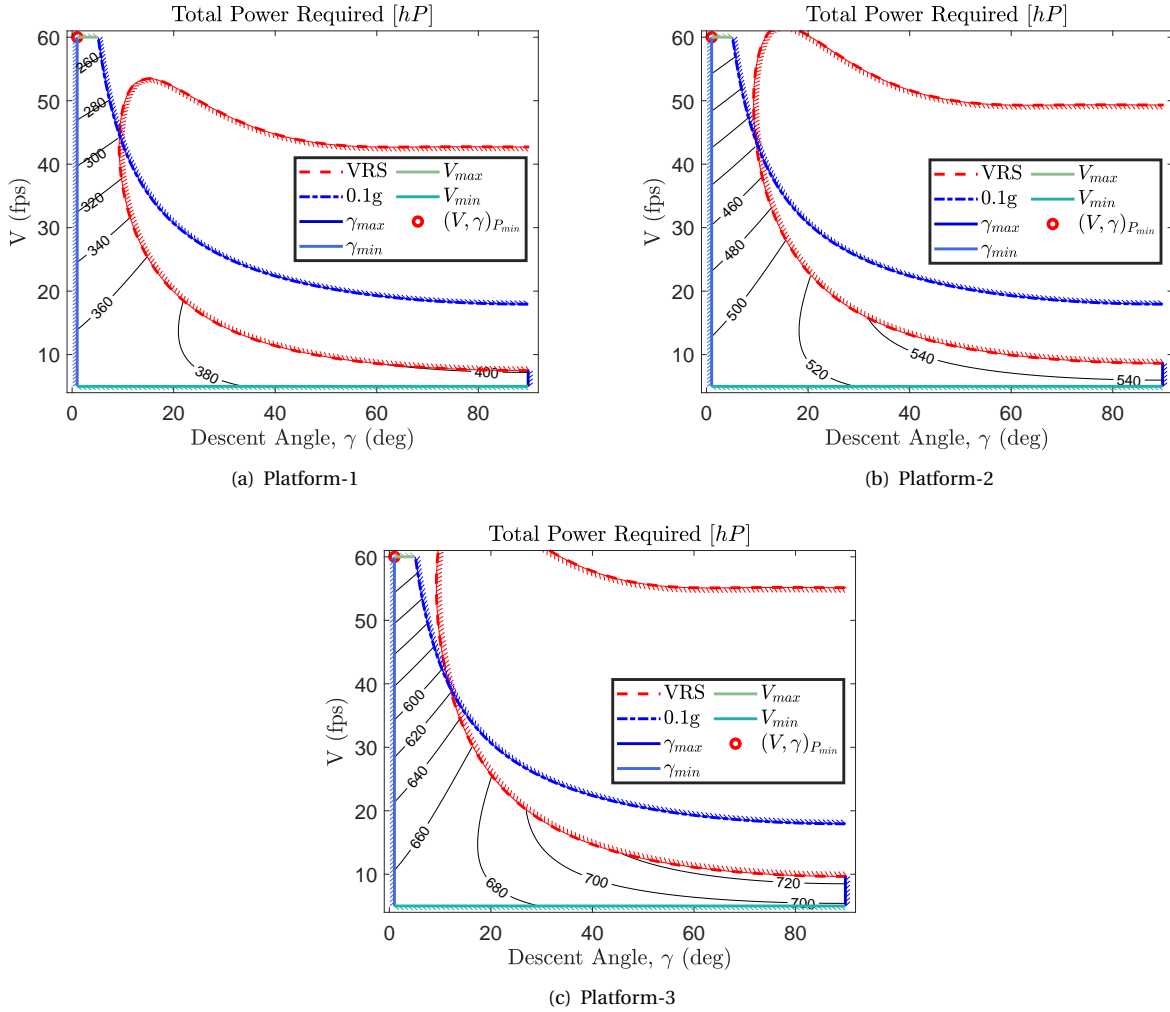


Figure 12 Contours for Required Power for Various Platforms

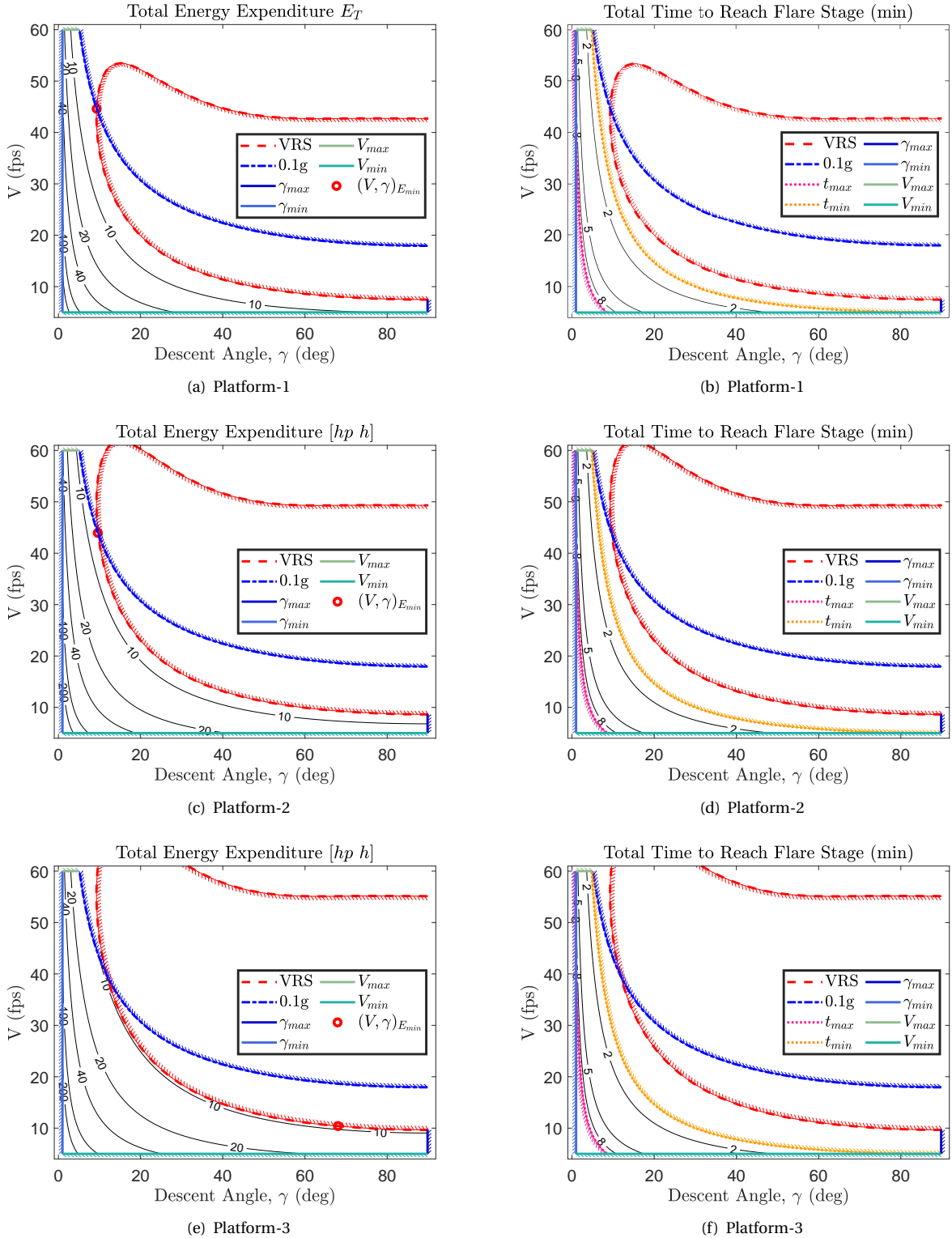


Figure 13 Contours for Energy and Time to Reach Flare Stage for Various Platform

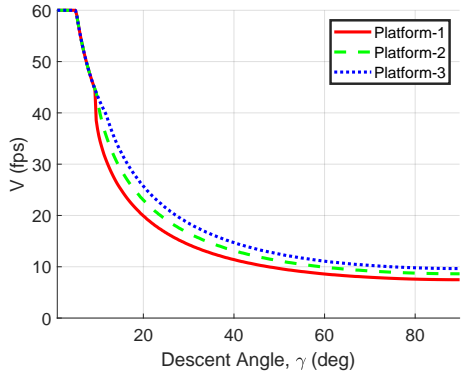


Figure 14 Speed Values that Minimize Energy Consumption for Given Descent Angle, γ , within Constraints

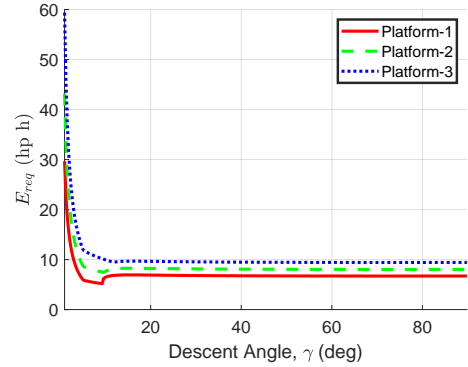
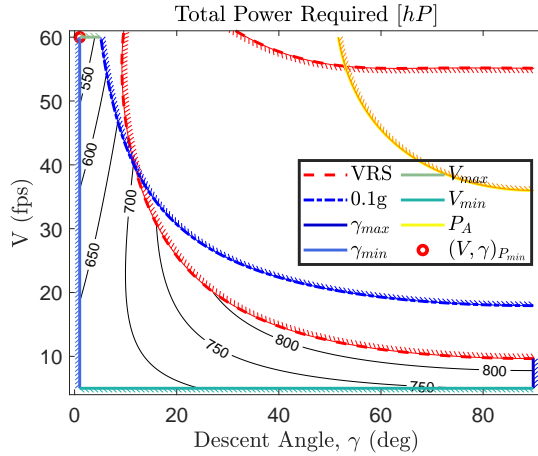
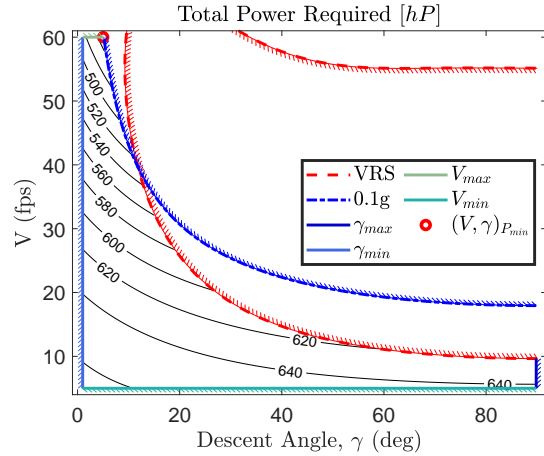


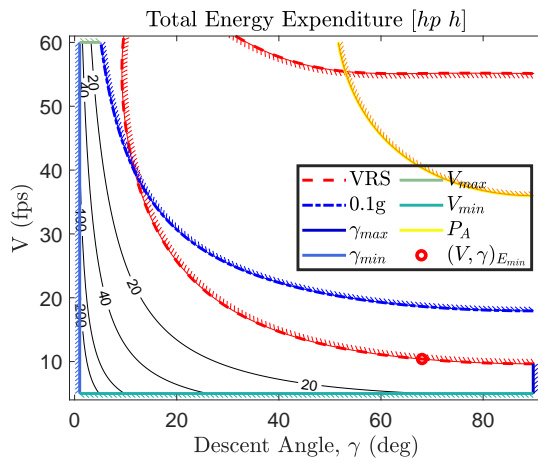
Figure 15 Minimized Energy Consumption for Given Descent Angle, γ , within Constraints



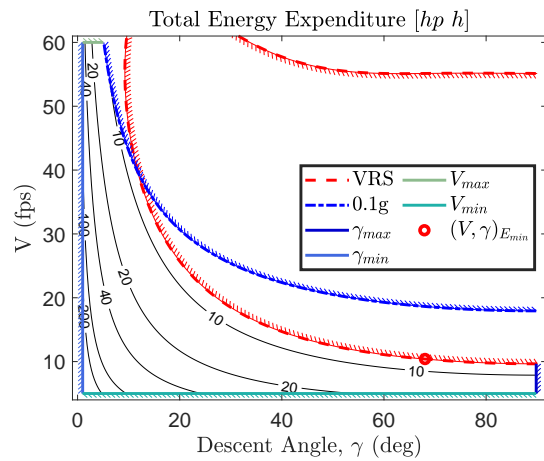
(a) Power Contours for PE-Gain (Climb)



(b) Power Contours for PE-Loss (Descent)



(c) Energy Contours for PE-Gain (Climb)



(d) Energy Contours for PE-Loss (Descent)

Figure 16 Contours for Power and Energy with Potential Energy Considerations for Platform 3

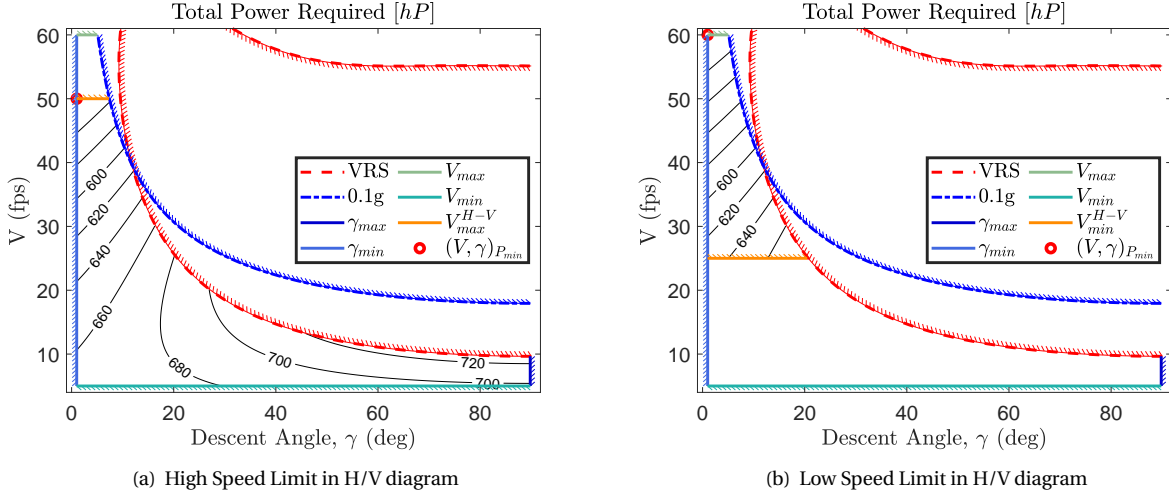


Figure 17 The Addition of Maximum and Minimum Speed Limits from H/V Diagram to Power Considerations for Platform 3

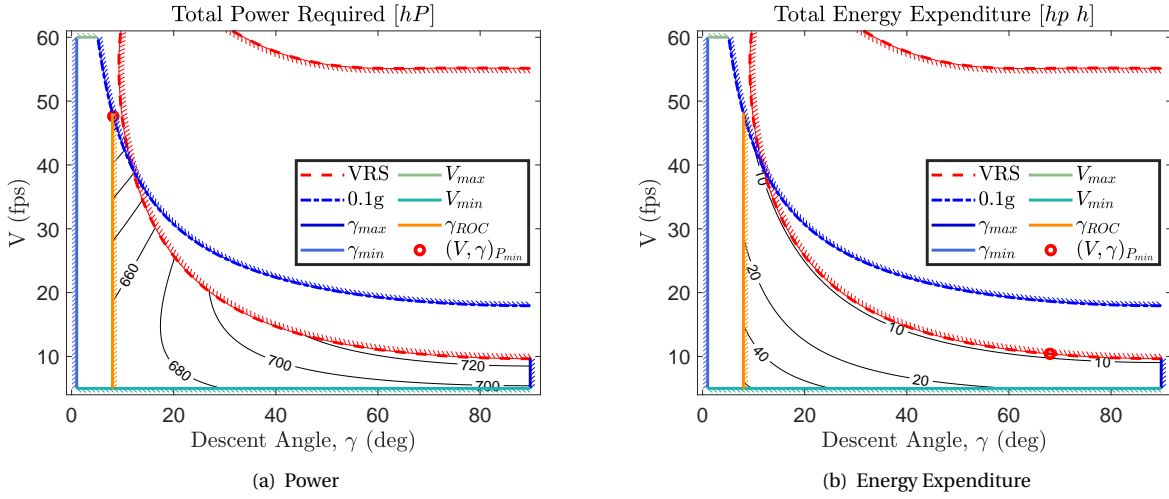


Figure 18 The Addition of Obstacle Clearance Limit as a Constraint for Platform 3

VI.B MONTE CARLO SIMULATION RESULTS

A series of Monte Carlo simulations are performed in order to develop a statistically meaningful ensemble of approach trajectories for the previously determined approach surfaces and speeds. Similar to the approach and transitional surfaces and FATO requirements in FAA Advisory Circular AC 150/5390-2C [2] for heliport designs, operational constraints can be applied on the simulations of VTOL aircraft. The speed-approach surface angle pairs which are the main parameters for simulations are varied within allowable limits based on the performance analysis to analyze the landing accuracy with fixed control architectures. The set of angle-speed pairs used are given in Table 3. The first two values are chosen based on assuming two upper limits regarding speed at the specified angles in accordance with the considerations of further safety and the constraints of preserving autorotation capability. All the other values are chosen by considering the minimum energy point and minimum time curve in the domain.

Table 3 Approach Angle and Speed Pairs

Approach Angle [deg] (γ_c)	2	5	20	40	60
Approach Speed [f/s] (V_c)	30	40	15	8	7
Theoretical time to reach flare [min] (t_t)	7.16	2.15	1.46	1.46	1.24

The elliptic error probables of touchdown points with probabilities of 50%, 70%, and 95% are shown in Figure 19 for an approach surface requirement with $\gamma_c = 5$ deg and $V_c = 40$ ft/s for light, moderate, and severe turbulence conditions. As can be observed, the semi major and semi-minor axes of the ellipses are increasing with severe wind turbulence. The changes of these axes with various glide angles can be seen in Figures 21(a) and 21(b). From light to moderate and from moderate to severe levels of turbulence, the axes increase for all cases. Especially, in terms of the semi-major axes radius, severe turbulence conditions cause unacceptably large deviations from the target point for several sets of simulations. For general light turbulence conditions, 95 % of the trajectories end up within a radius of 20 - 30 ft. The control effort spent during the simulations can be tracked as another metric to analyze the influence of different approach parameter pairs. Figure 20 indicates the change of the sum of control effort spent in actuators normalized with the approach surface angles and the corresponding speed values. The normalization is performed with respect to the minimum effort spent among all cases of turbulence levels. Results show that the smallest values are obtained for light turbulence when compared to others as expected. At higher angles for each turbulence level in the simulations for both longitudinal control channels, a significant drop of normalized control effort is observed. The minimum value is obtained at an approach angle of 60 degrees and with light turbulence.

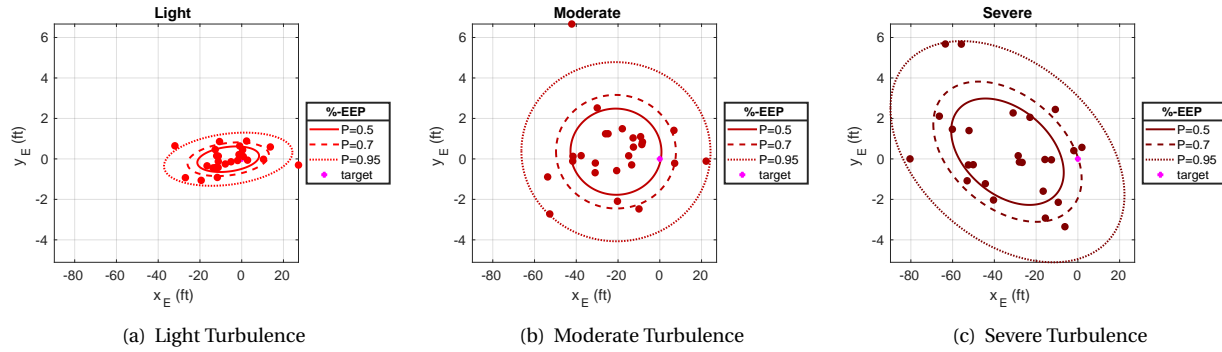


Figure 19 Error Elliptical Probables for $\gamma_c = 5$ deg and $V_c = 40$ ft/s

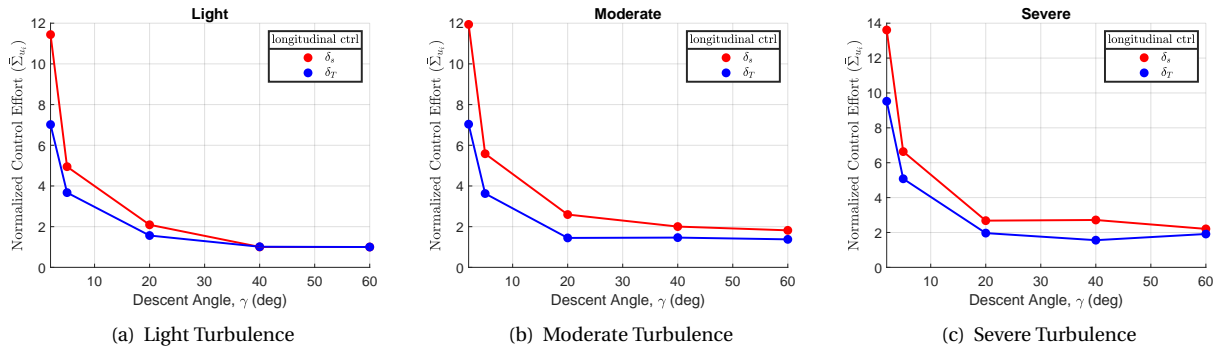


Figure 20 Normalized Control Effort spent for Various Turbulence Levels

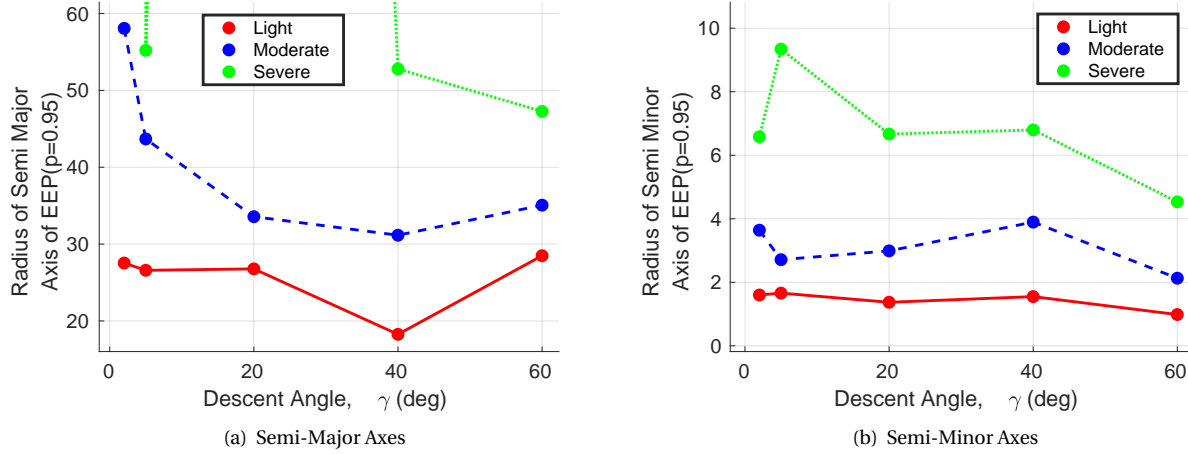


Figure 21 Change of Radii of Semi-Minor and Semi-Major Axes of Error Elliptical Probables

The approach speed changes are shown in Figure 22(a) for the simulation parameters of $\gamma_c = 60$ deg and $V_c = 7$ ft/s and for various turbulence levels. The greater severity levels of turbulence result in more dispersion from the commanded values and the mean of recordings at a given time. The step-by-step change of the speeds during flare and the transition from cruise to approach can be detected in these figures. The change of approach speed can be observed from speed versus approach angle plots in Figures 23. The swirls correspond to the converging behavior of the system to desired values fed from flight control. The descent angle shown for this case is -2 degrees. During the approach, a speed of 30 ft/s is intended. In the flare stage, this value is gradually decreased as indicated by other swirling behaviour at lower speeds.

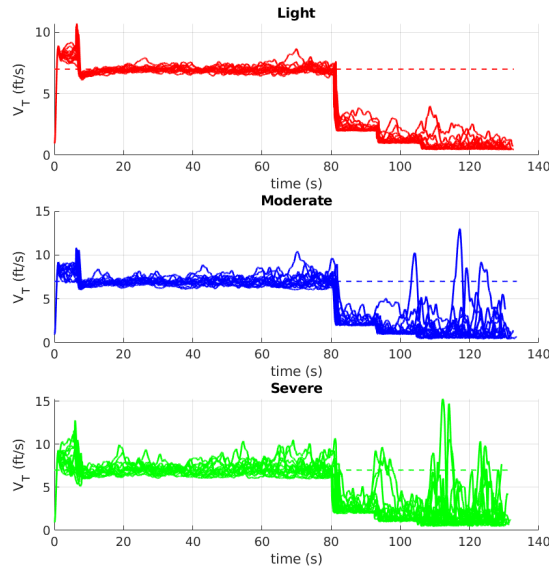


Figure 22 Change of Approach Speed for $\gamma_c = 60$ deg and $V_c = 7$ ft/s and Various Turbulence Levels

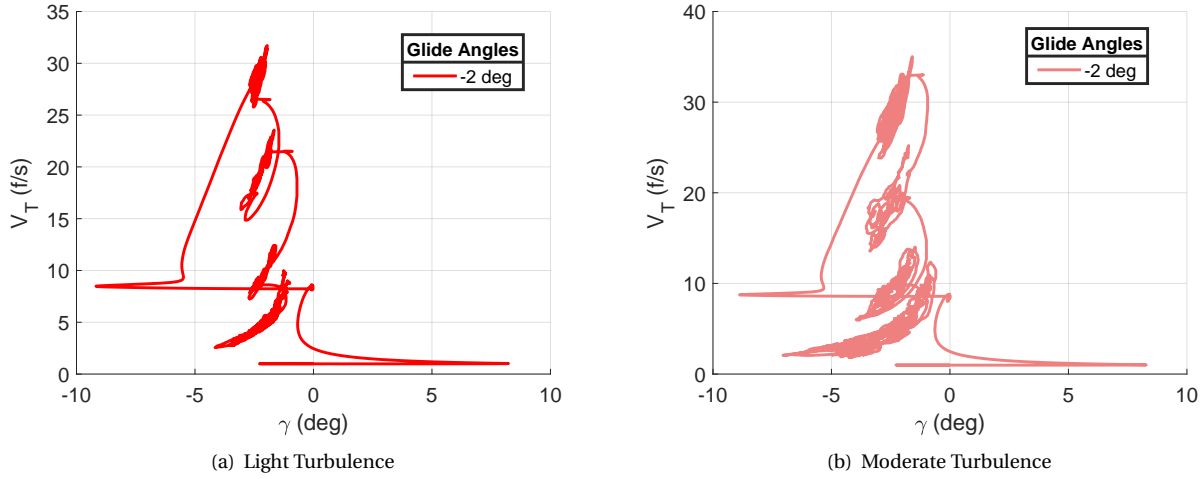


Figure 23 Approach Speed vs. Approach Angle for Light and Moderate Turbulence Levels

VII CONCLUSIONS

In this paper, we presented methods to examine performance and landing accuracy during approach to vertiports. First, we conducted a performance analysis for representative UAM eVTOL vehicles along landing approach surfaces. This analysis attempted to develop methods to understand the influence of changing approach angles and speeds on the vehicle performance, passenger comfort, and procedural requirements. Several constraints such as vortex ring state boundaries, power availability, obstacle clearance, and acceleration limits were considered. Although constraints on classical H/V diagrams can be neglected due to the functionally redundant propulsion units anticipated for most eVTOLs, we investigated the influence of the constraints from H/V diagrams on the performance. For VRS boundary, the influence of disk loading was also explored. From this analysis, approach speeds were selected for given approach angles within the feasible and safe operation envelope with minimal energy and time considerations. The selected surfaces with constant speeds and constant angles were used in the second part of the paper for Monte Carlo simulations to evaluate landing accuracy. These simulations attempted to facilitate the exploration of the vertiport FATO area size and were analyzed statistically. The study was carried out based on a notional eVTOL derived by scaling the XC-142A. For the influence of weather, a turbulence model was integrated into the simulation modules. The results provided elliptical error probabilities for the landing accuracy of different approach surfaces and weather conditions. Normalized control efforts for these surfaces and changes to the radii of these error ellipses were also noted.

REFERENCES

- [1] Holden, J., and Goel, N., "Uber Elevate: Fast-Forwarding to a Future of On-Demand Urban Air Transportation," , September 27, 2016. Retrieved from uber.com/elevate.pdf on May 7, 2019.
- [2] "Federal Aviation Administration FAA AC 150/5390-2C: Heliport Design," , April 24, 2012. Retrieved from faa.gov/documentLibrary/media/Advisory_Circular/150_5390_2c.pdf on May 7, 2019.
- [3] "HeliOffshore Operational Effectiveness Approach Path Management Guidelines," , July 2017. Issue 1, version 3.0. Retrieved from helioffshore.org/wp-content/uploads/2016/07/Approach-Management-Guidelines-v2.pdf on May 20, 2019.
- [4] "Federal Aviation Administration United States Standard for Terminal Instrument Procedures (TERPS)," , February 16, 2018. Retrieved from faa.gov/documentLibrary/media/Order/Order_8260.3D_vs3.pdf on May 7, 2019.
- [5] McRuer, D. T., Ashkenas, I., and Graham, D., "Aircraft Dynamics and Automatic Control," , 1968. Naval Air Systems Command Department of the Navy Technical Report No. 129-1.

- [6] Fredericks, W. J., "Impact of Operational Requirements on Intra-Urban VTOL Conceptual Design," , 2016. Oral presentation in 16th AIAA Aviation Technology, Integration, and Operations Conference.
- [7] Franklin, J. A., *Dynamics, Control, and Flying Qualities of V/STOL Aircraft*, AIAA Education Series, 2002.
- [8] Silva, C., Johnson, W., Antcliff, K. R., and Patterson, M. D., "VTOL Urban Air Mobility Concept Vehicles for Technology Development," *2018 Aviation Technology, Integration, and Operations Conference*, AIAA, 2018.
- [9] Johnson, W., Silva, C., and Solis, E., "Concept Vehicles for VTOL Air Taxi Operations," *AHS Technical Conference on Aeromechanics Design for Transformative Vertical Flight*, AHS, 2018. San Fransisco, CA.
- [10] Johnson, W., and Silva, C., "Observations from Exploration of VTOL Urban Air Mobility Designs," , 2018. Oral presentation in 7th Asian/Australian Rotorcraft Forum; 30 Oct. - 1 Nov. 2018; Jeju Island; Republic of Korea.
- [11] *Bartini: The flying car*, 2019. Retrieved from bartini.aero/ on May 7, 2019.
- [12] *Transcend-air Vy 400*, 2019. Retrieved from transcend.aero/aircraft on May 7, 2019.
- [13] *Design Specifications Volocopter 2X*, 2017. Retrieved from volocopter.com/assets/pdf/2017_04_Design_specifications_2X.pdf on May 7, 2019.
- [14] *Carter 2+2 Place Personal Air Vehicle*, 2018. Retrieved from cartercopters.com/pav.html on May 7, 2019.
- [15] Johnson, W., *Helicopter Theory*, Dover Books on Aeronautical Engineering Series, Dover Publications, 1994.
- [16] Chen, C., "Development of a Simplified Inflow Model for a Helicopter Rotor in Descent Flight," Ph.D. thesis, Georgia Institute of Technology, August 2006.
- [17] Heyson, H. H., "Momentum Analysis of Helicopters and Autogyros in Inclined Descent, with Comments on Operational Restrctions," , 1975. NASA Technical Note, NASA TN D-7917.
- [18] Johnson, W., *Rotorcraft Aeromechanics*, Cambridge Aerospace Series, Cambridge University Press, 2013.
- [19] Johnson, W., "NDARC - NASA Design and Analysis of Rotorcraft," , April 01, 2015. NASA/TP-2015-218751, ARC-E-DAA-TN22623.
- [20] "R22 Pilot's Operating Handbook and FAA approved Rotorcraft Flight Manual RTR 061," , 2016. Robinson Helicopter Company.
- [21] Vuichard, C., "More Safety for Pilots with Vuichard Techniques," , 2019.
- [22] Foster, J. V., and Hartman, D., "High-Fidelity Multi-Rotor Unmanned Aircraft System Simulation Development for Trajectory Prediction Under Off-Nominal Flight Dynamics," *17th AIAA Aviation Technology, Integration, and Operations Conference*, AIAA, 2017.
- [23] Johnson, W., "Model for Vortex Ring State Influence on Rotorcraft Flight," , December 2005. NASA Technical Note, NASAITP-2005-213477.
- [24] Reuter, F., "The Volocopter by e-volo GmbH," , March 9, 2016.
- [25] Taghizad, A., and Binet, L., "Assessment of VRS Risk during Steep Approaches," *American Helicopter Society 62nd annual Forum*, AHS, 2006.
- [26] Newman, S., Brown, R., Perry, J., Lewis, S., Orchard, M., and Modha, A., "Predicting the Onset of Wake Breakdown for Rotors in Descending Flight," *Journal of the American Helicopter Society*, Vol. 48, No. 1, 2003, pp. 28–38.
- [27] Abildgaard, M., and Binet, L., "Active Sidesticks used for Vortex RIing State Avoidance," *35th European Rotorcraft Forum*, DGLR, 2009.
- [28] Gornstein, R. J., Shultz, W. M., and Stair, L. D., "Marine vehicle ride quality," *NASA Langley Research Center Symposium on Vehicle Ride Quality*, NASA, 1972, pp. 197–209.
- [29] Leatherwood, J. D., Clevenson, S. A., and Hollenbaugh, D. D., "Evaluation of Ride Quality Prediction Methods for Helicopter Interior Noise and Vibration Environments," , 1984. NASA Technical Paper 2261, AVSCOM Technical Report 84-D-2.

- [30] Griffin, M. J., "A Review of Ride Comfort Studies in the United Kingdom," *Ride Quality Symposium*, NASA, 1975, pp. 471–499. NASA TM X-3295, DOT-TSC-OST-75-40.
- [31] McKenzie, J. R., and Brumaghin, S. H., "Review of Ride Quality Technology Needs of Industry and User Groups," *Ride Quality Symposium*, NASA, 1975, pp. 5–30. NASA TM X-3295, DOT-TSC-OST-75-40.
- [32] Holloway, R. B., and Brumaghin, S. H., "Tests and analyses applicable to passenger ride quality of large transport aircraft," *NASA Langley Research Center Symposium on Vehicle Ride Quality*, NASA, 1972, pp. 91–113.
- [33] *Tiltwing Prototype LTV XC-142A*, NASA Langley Research Center, 2001. Retrieved from crgis.ndc.nasa.gov/historic/File:E1-2001-00399.jpg on May 7, 2019.
- [34] Caughey, D. A., "Aircraft Dynamics and Automatic Control Course Notes for M & AE 5070," , 2011. Sibley School of Mechanical and Aerospace Engineering, Cornell University, Ithaca, NY 14853-7501.
- [35] Labows, S. J., "UH-60 Black Hawk Disturbance Rejection Study for Hover/Low Speed Handling Qualities and Turbulence Modeling," Master's thesis, Naval Postgraduate School, Monterey, California, March 2000.
- [36] Costello, M., Gaonkar, G. H., Prasad, J. V. R., and Schrage, D. P., "Some Issues on Modeling Atmospheric Turbulence Experienced by Helicopter Rotor Blades," *Journal of the American Helicopter Society*, 1992, pp. 71–75.
- [37] Dahl, H. J., and Faulkner, A. J., "Helicopter Simulation in Atmospheric Turbulence," *4th European Rotorcraft Forum, Stresa, Italy*, 1978.
- [38] Hess, R. A., "Rotorcraft Handling Qualities in Turbulence," *Journal of Guidance, Control, and Dynamics*, Vol. 18, No. 1, 1995, pp. 39–45.
- [39] "MIL-STD-1797A, Flying Qualities of Piloted Aircraft," , December 19, 1997. Department of Defense.